RESEARCH ARTICLE | FEBRUARY 02 2024

### Pendant drop motion and stability in vertical airflow ⊘

Jacob D. Dockery <sup>®</sup> ; Duygu Yilmaz Aydin <sup>®</sup> ; Andrew K. Dickerson ■ <sup>®</sup>



Physics of Fluids 36, 027107 (2024) https://doi.org/10.1063/5.0187843





CrossMark





# Pendant drop motion and stability in vertical airflow

Cite as: Phys. Fluids **36**, 027107 (2024); doi: 10.1063/5.0187843 Submitted: 16 November 2023 · Accepted: 5 January 2024 · Published Online: 2 February 2024







Jacob D. Dockery,<sup>1</sup> 🙃 Duygu Yilmaz Aydin,<sup>1,2</sup> 🕞 and Andrew K. Dickerson<sup>1,a)</sup> 🙃



#### **AFFILIATIONS**

<sup>1</sup>Mechanical, Aerospace, and Biomedical Engineering, University of Tennessee, Knoxville, Tennessee 37996-2210, USA

#### **ABSTRACT**

When exposed to an ascending flow, pendant drops oscillate at magnitudes determined by windspeed, drop diameter, and needle diameter. In this study, we investigate the retention stability and oscillations of pendant drops in a vertical wind tunnel. Oscillation is captured by a high-speed camera for a drop Reynolds number Re = 200-3000. Drops at Re  $\leq$  1000 oscillate up to 12 times the frequency of drops with high Re. Increasing windspeed enables larger volume drops to remain attached to the needles above Re = 500. We categorize drop dynamics into seven behavioral modes according to the plane of rotation and deformation of shape. Video frame aggregation permits the determination of a static, characteristic shape of our highly dynamic drops. Such a shape provides a hydraulic diameter and the evaluation of the volume swept by the oscillating drops with time. The maximum swept volume per unit drop volume occurs at Re = 600, corresponding to the peak in angular velocity.

Published under an exclusive license by AIP Publishing. https://doi.org/10.1063/5.0187843

#### I. INTRODUCTION

From dripping faucets to dripping noses, pendant drops are commonplace to the human experience, and their teardrop shape inspires how most inaccurately visualize raindrop shapes. Pendant drops are of importance across a diversity of fields such as pharmaceuticals, 1,3 food,<sup>3,4</sup> material characterization,<sup>5,6</sup> environmental science,<sup>7</sup> and labon-a-chip devices.<sup>8,9</sup> The fundamental physics of pendant drops have been studied in the context of the transition from dripping to jetting, 10 their pinch-off, 11,12 vibration, 13 interactions with microjets, 14 and how their shape unveils liquid surface tension. 15,16 However, these investigations have been carried out in quiescent conditions, stymieing the application of pendant drops in more dynamic environments. In this study, we subject pendant drops, extruded by straight-cut needles, to an ascending airflow parallel to the needle axis and gravity. The airflow alters the size of a drop a needle can support and induces drop oscillation and dynamic deformation as seen in Fig. 1.

Perhaps the most relevant dynamic systems to ours, that have been studied, are free-falling and levitating drops. 17-26 The behavior of a free-falling drop is dictated by shape oscillation, size, and internal circulation.<sup>26</sup> For small raindrops, below 1 mm in diameter, drops are spherical. When the drop diameter surpasses 1 mm, raindrops flatten and oscillate in a manner governed by the internal circulation of the drop. Such internal circulation and periodic shape deformation are

incited by the passing airflow through vortex shedding.<sup>27</sup> The oscillatory motion of a falling drop can be sorted into behavioral modes defined by axisymmetric, horizontal, and transverse modes or combinations thereof.2

Pendant drops differ from raindrops because their motion is constrained, complicating the physics and resulting in a rich spectrum of dynamic behavior. Investigations regarding the behavior of pendant and sessile drops in response to external forcing are relatively limited. The dynamics of pendant and sessile drops have been induced by vibrating rods, <sup>28</sup> electric fields, <sup>29–32</sup> and acoustics. <sup>33–35</sup> In the presence of an acoustic field, pendant drops exhibit longitudinal, lateral, and rotational modes, the lowest of which is drop rotation about the gravitational axis similar to a conical pendulum. For pendant drops under an acoustic field, drop rotational frequency decreases with increasing drop size.<sup>34</sup> For drop dynamics in response to the vertical, sinusoidal motion of the capillary support, the resonant frequency of oscillation is highly influenced by drop size, and a decrease in fluid viscosity increases drop deformation. Such shape deformation is determined by a balance between surface tension, capillary pressure, and viscous shear stress induced by the oscillating rod.<sup>2</sup>

To the authors' knowledge, no studies have examined the oscillations of pendant drops in response to vertical airflow. In this experimental study, we measure oscillation and deformation characteristics

<sup>&</sup>lt;sup>2</sup>Bioengineering, Malatya Turgut Ozal University, Malatya, Turkey

a) Author to whom correspondence should be addressed: ad@utk.edu

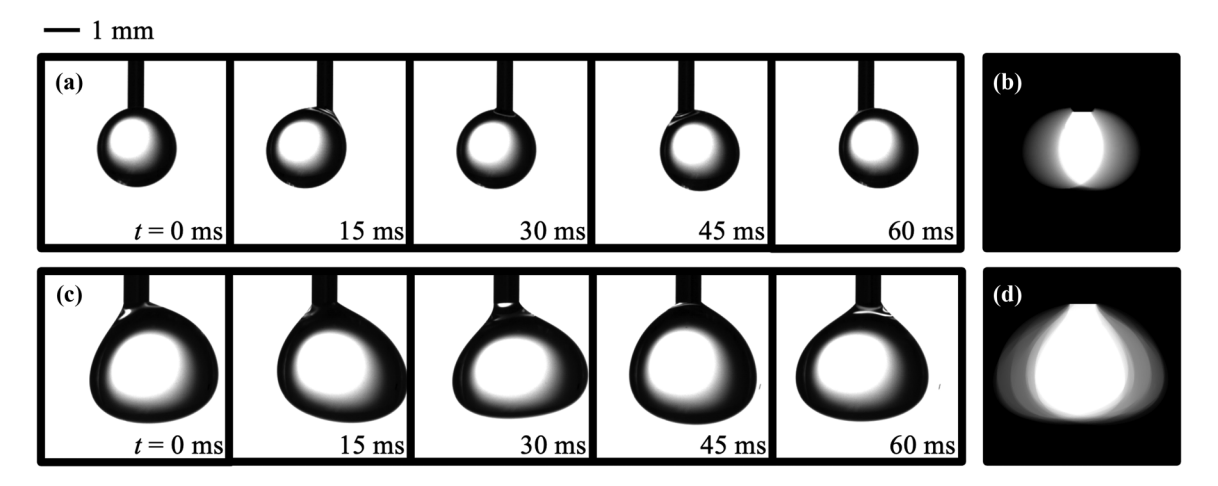


**FIG. 1.** Pendant drops oscillate and deform in vertical airflow. (a) Time sequence of a drop oscillating in airflow on a needle with diameter  $D_N = 0.42$  mm. (b) Aggregated binarized shadowgraph of motion in (a). (c) Time sequence of a drop experiencing periodic shape deformation shape oscillating in airflow with  $D_N = 0.71$  mm. (d) Aggregated binarized shadowgraph of motion in (c).

for pendant drops of various sizes, needle diameters, surface tension, and ascending flow velocities. We describe the dynamics of oscillation by two dimensionless groups, the Reynolds number  ${\rm Re}=\rho UD_{\rm H}/\mu=200-3000$  and a modified Strouhal number  ${\rm St}=\omega D_{\rm H}/2\pi U$ , where U is airflow velocity, air density and dynamic viscosity are  $\rho=1.293~{\rm kg/m^3}$  and  $\mu=0.0184~{\rm cP}$  at 20°C, respectively, and  $\omega$  is the angular velocity of a rotating pendant drop. The drop hydraulic diameter  $D_{\rm H}=6\,\mathcal{V}^{1/3}/\pi$ , where V is drop volume. The use of dimensionless groups to describe behavior and performance simplifies the use of pendant drops in future airflow-based studies.

#### II. EXPERIMENTAL METHODS

In this study, pendant drops of distilled water ranging in volume from 2 to 50  $\mu$ l are observed on supports of needle outer diameter  $D_{\rm N}=0.42,~0.71,~$  and 0.92~ mm at 17 vertical wind tunnel velocities U=1-9~ m/s. Laminar, vertical airflow is delivered to hanging pendant drops by the pull-type vertical wind tunnel shown in Fig. 2. Ambient lab air is pulled by an 8 in. duct fan into the lower cross section of the tunnel and passes through a HEPA filter, contraction section, and honeycomb laminarizer before entering the contraction section. Fan speed is modulated by an ITech IT-M7721L variable AC

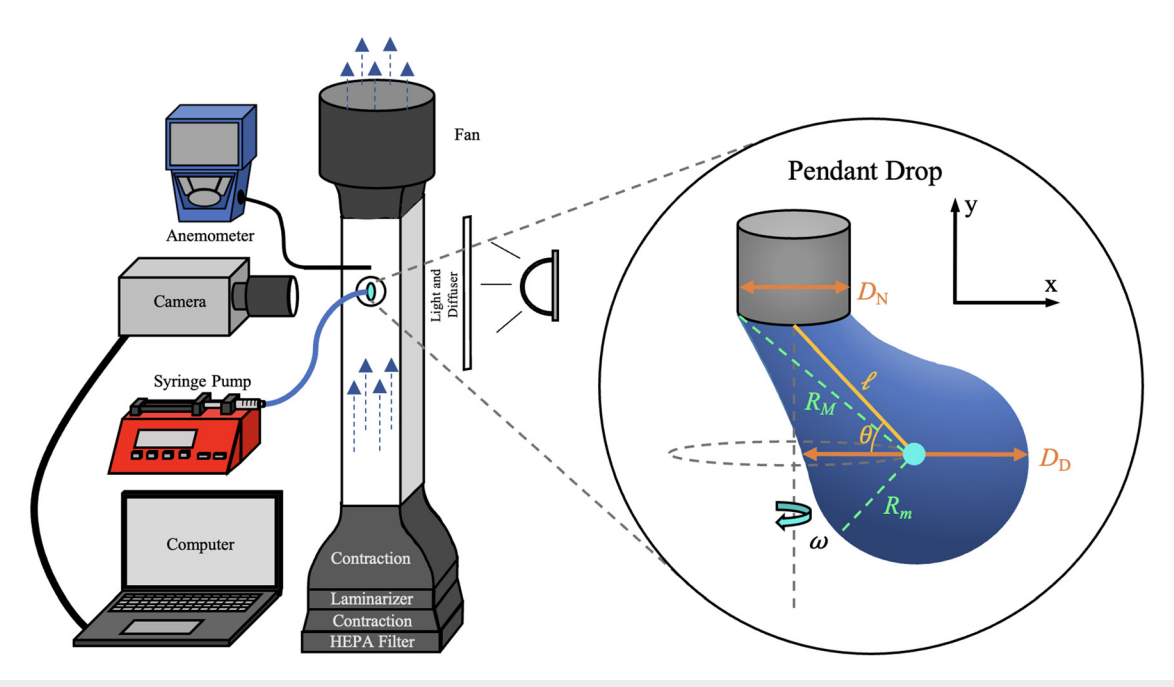


FIG. 2. Schematic of the experimental setup. The zoom bubble showcases the pertinent dimensions of a pendant drop in motion.

power supply. The half-width f of the two-dimensional contraction in centimeters is defined by  $f(y) = -1.2 \times 10^{-7} y^6 + 8.9 \times 10^{-6} y^5 -1.7 \times 10^{-4} y^4 + 15$ , where y (cm) is the axial dimension of the contraction and y = 0 corresponds to the contraction inlet.<sup>36</sup> The ascending laminar flow traverses the acrylic observational section measuring  $12 \times 12$  cm<sup>2</sup>. External vibrations imposed on the tunnel are abated by vibration-dampening pads.

The velocity of the ascending flow is measured by a TSI Velocicalc anemometer with 0.01 m/s precision. A prescribed volume of distilled water is pumped out of the needle by a New Era NE-800 syringe pump to form the pendant drop. Drops of reduced surface tension are produced by the addition of Triton X-100 (Aqua Solutions, Inc.), a nonionic surfactant, to distilled water. An interfacial tensiometer (Dataphysics OCA 15EC) is used to measure the surface tension of the solution. In select experiments, needles are made hydrophobic by coating their exterior with Glaco Mirror Coat Zero water repellent, producing drops with contact angles of  $118^{\circ} \pm 3^{\circ}$ , number of measurements N=7, using the sessile drop method. Drops inside are backlit and filmed by a Photron Nova S6 fitted with a 105-mm 1:2.8 Sigma lens at 1000 fps. Three replicates are conducted for each experimental condition.

## III. IMAGE INTERPRETATION AND BEHAVORIAL MODES

Analysis and image binarization are performed by bespoke code in MATLAB. From binarized images, we measure drop variables listed in Fig. 2 except for needle diameter  $D_{\rm N}$ , which serves as the physical scale. Drop volume V is calculated using the second theorem of Pappus<sup>37</sup> at the instant when the cross-sectional image of the drop is intersected by the plane parallel to the lens, cross-sectioning the needle. Rotational frequency  $\omega$  is quantified by tracking the lateral position of the centroid  $x_0$  and averaging at least 1.5 periods.

Pendant drops rotate and experience periodic shape deformation in the presence of an ascending flow. The axis of rotation about which the pendant drop rotates can be static or dynamic, a behavior that has no analogy in falling drops. The ratio  $D_{\rm H}/4=A/P$ , where A is the cross-sectional area of the drop and P is the corresponding perimeter, provides a convenient threshold between static and dynamic axis behavior. The criterion for a dynamic axis of rotation is thus  $y_0P > A$ , an inequality relating the area of a shape formed by the product  $y_0P$  to A, where  $y_0$  is the amplitude of oscillation of the drop centroid in the direction of gravity. The bouncing drops of dynamic axes have larger  $y_0$  values such that  $y_0 > D_{\rm H}/4$  as the drops circumnavigate the needle. Drops with a static axis of rotation have a center of mass that deviates  $y_0 < D_{\rm H}/4$ .

To monitor the shape of the drop over time, we introduce a shape factor to capture the instantaneous shape of the drop  $R_{\rm M}/R_{\rm m}$ , where  $R_{\rm M}$  and  $R_{\rm m}$  are the maximum and minimum distances from the drop centroid to the two-dimensional drop boundary, as labeled in Fig. 2. The magnitude of  $R_{\rm M}/R_{\rm m}$  is periodic with time, the frequency of which, shape factor frequency  $\Gamma$ , yields insight into the presence of deformation, or lack thereof. Drops that do not change shape as they rotate have a nonzero shape factor frequency, a result of our two-dimensional view. By dividing  $\Gamma$  by rotational frequency  $\omega/2\pi$ , we create a dimensionless shape deformation factor  $\Omega=2\pi\Gamma/\omega$ . Geometrically, when  $\Omega\approx 2$ , the shape of the pendant drop is static as the frequency of rotation is half that of the shape factor frequency. When  $\Omega\lesssim 1.85$   $\Omega\lesssim 2.15$ , the drop has periodic shape deformations

as the shape factor frequency and rotational frequency are mismatched.

We categorize the rotational and deformational behavior of pendant drops into seven modes dependent upon the axis of rotation dynamics and periodic shape deformations of the drop, as shown in Fig. 3(a). A binary system indicates the presence of rotation, rotation axis migration, and the relative magnitude of shape deformation  $(\alpha, \beta) = (axis of rotation, shape deformation)$ . In the absence of drop rotation,  $\alpha = 0$ , and in the absence of periodic shape deformation,  $\beta = 0$ . For example, a static drop hanging from a needle in quiescent conditions is in mode (0, 0). We define that if  $x_0 < 2$  pixels p, the drop is not rotating and is ascribed  $\alpha = 0$ . If the pendant drop is rotating or periodically deforming,  $\alpha$  or  $\beta$  may equal 1a or 1b. The binary 1 indicates that the drop is rotating or deforming, whereas the modifiers "a" and "b" determine the quality of rotation and deformation. For  $\alpha = 1a, 1b$ , the drop has a static or dynamic axis of rotation, respectively. For  $\beta = 1a, 1b$ , the drop experiences periodic shape deformations of magnitudes  $2.15 \le \Omega < 4.5$  or  $\Omega \ge 4.5$ , respectively. For each behavioral mode in Fig. 3(a), we show a representative schematic and an aggregated binarized shadowgraph (ABS) of a drop. The ABS is created by normalizing the summation of every binarized frame of the oscillating drop, allowing for an averaged spatiotemporal diagram of a dynamic drop. In an ABS, the brightness of each pixel indicates how often the drop resides in that particular location on a timeaveraged basis. In each corresponding schematic, dark blue circles characterize drops of stable shape, while light blue ellipses represent drops experiencing periodic shape deformities. Drop rotation paths are shown as either singular (1a) or multiple (1b), in which the axis of rotation migrates as the drop rotates. Drop behavior becomes increasingly dynamic as the ascending flow velocity increases, as observed in Fig. 3(a). At U = 1 m/s, all drops are of mode (0, 0). At flow velocities  $U \ge 2$  m/s, all drops experience rotational motion on each needle. We plot the most dominant behavioral mode for each needle across U in Fig. 3(b). The most common behavioral mode observed is mode (1a,0). In (1a, 0), a drop of stable shape rotates about the needle with a static rotational axis. The rotational path of the drop centroid in this mode is analogous to that of a conical pendulum, similar to the lowest oscillation mode of a pendant drop in an acoustic field.<sup>34</sup> Here, any internal circulation dissipates within the drop and normal stresses acting in the wake of the drop are insufficient to induce periodic shape deformation. At U = 8 m/s, mode (1b, 0) is dominant. In (1b, 0), a drop of stable shape rotates about the needle with a dynamic axis of rotation. Only at our highest tested windspeed, U = 9 m/s, does the dominant mode include shape deformities. For  $D_{\rm N}=0.61$  mm, (1a, 1b) is the dominant mode. In this mode, the drop weight is substantially large such that surface tension is incapable of maintaining a uniform drop curvature. Though air drag is applied to a time-variant cross-sectional area, the change in the drop cross-sectional area seen by the ascending flow is not sufficient to induce periodic bouncing. Similarly, for  $D_{\rm N}=0.41~{\rm mm}$  at  $U\!=\!9~{\rm m/s}$ , shape instabilities are present, and the axis of rotation is dynamic. The cross-sectional area upon which the drag force acts dramatically varies with time, causing the drop to bounce. The difference in mode for the same U but differing  $D_N$  is likely due to the discrepancy in capillary force and the size of the body in the wake of the drop.

The observance of periodic shape deformation for an oscillating drop correlates with the amplitude of oscillation  $x_0$  and needle diameter. We plot the relationship between needle-relative amplitude  $x_0/D_{\rm N}$ 

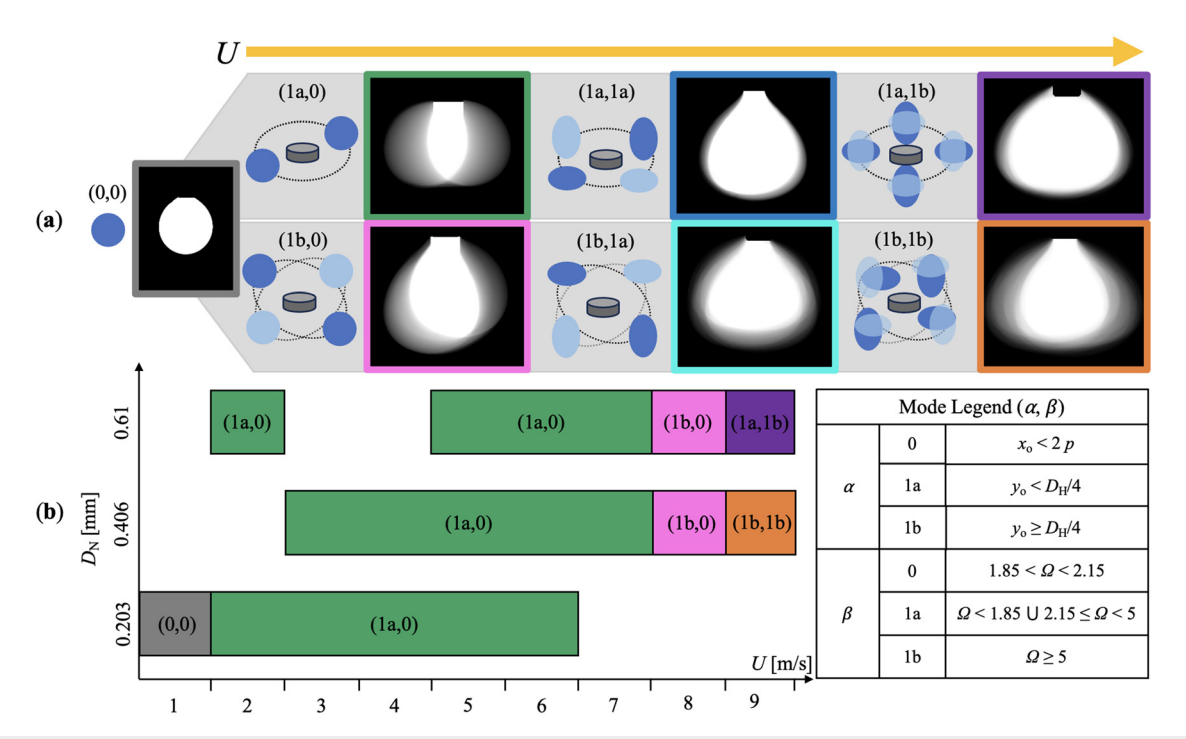
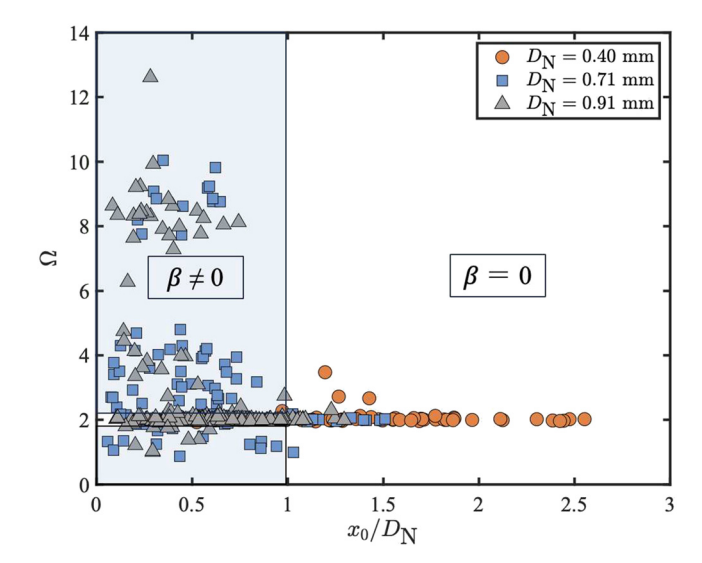


FIG. 3. Drop and needle size, and ascending flow velocity determine the emergence of discrete behavioral modes. Panel (a) schematizes how behavioral modes emerge as velocity increases. For each mode, the left-hand diagram shows a generalized representation of rotation planes, paths, and drop deformations along the paths around the needle. The right-hand images for each mode are aggregated binarized shadowgraphs (ABS) simultaneously capturing drop rotation and deformation. Panel (b) is a graphical representation of mode dominance for a given needle size and wind speed. The primary colors of the bar correspond to the frames surrounding ABS in (a). The physical measurements distinguishing modes are provided in the mode legend where alpha and beta placeholders for the axis of rotation and shape deformation, respectively. Multimedia available online.

and  $\Omega$  in Fig. 4. In general, no periodic shape deformation is observed for pendant drops with oscillation amplitudes that exceed the needle bounds. For the majority (64%) of drop sizes and flow velocities tested,  $\beta=0$ . Barring four outliers, the condition of  $\beta=1$  requires  $x_0/D_{\rm N}<1$ .

#### IV. DROP OSCILLATION

Pendant drops oscillate in the presence of ascending flows. We measure the angular velocity  $\omega$  of pendant drops supported by three test needles across a range of windspeeds U = 1 - 9 m/s at 1-m/s intervals. The variation in needle size, drop volume, and windspeed creates 139 unique test conditions and is constrained by the size drop a needle can support (Sec. V). Pendant drops have a Reynolds number  $Re = \rho UD_H/\mu$ , where air density and dynamic viscosity are  $\rho = 1.293 \text{ kg/m}^3$  and  $\mu = 0.0184 \text{ cP}$ , respectively, and drop hydraulic diameter  $D_{\rm H}=6V^{1/3}/\pi$ . For Re  $\gtrsim$  500, the angular velocity of pendant drops decreases with increasing Re as shown in Fig. 5(a). Reynolds number contours, a slight deviation in Re due to a change in D<sub>H</sub> on a fixed needle, indicate that smaller drops oscillate faster than larger drops, as the minima and maxima of  $\omega$  for each contour correspond to the smallest and largest drop size tested. Below Re  $\approx$  1500, drops attached to differing needle diameters D<sub>N</sub> and comparable Re rotate at varying  $\omega$ . The peak in  $\omega \approx 360$  rad/s occurs at Re  $\approx 500$  on  $D_{\rm N}=0.91$  mm, 4 and 2.5 times the angular velocity for drops of comparable Re supported by  $D_{\rm N}=0.40\,{\rm and}\,0.71\,$  mm, respectively. Drops will oscillate faster when adhered to larger needles for  $500 \lesssim \text{Re} \lesssim 1500$ . The discrepancy between angular velocities for drops of comparable Reynolds numbers indicates that needle diameter significantly influences drop oscillation, likely due to changes in the drop wake structure.



**FIG. 4.** Pendant drops may experience shape deformation when exposed to an ascending flow. Plot of  $\Omega$  vs needle-relative amplitude.

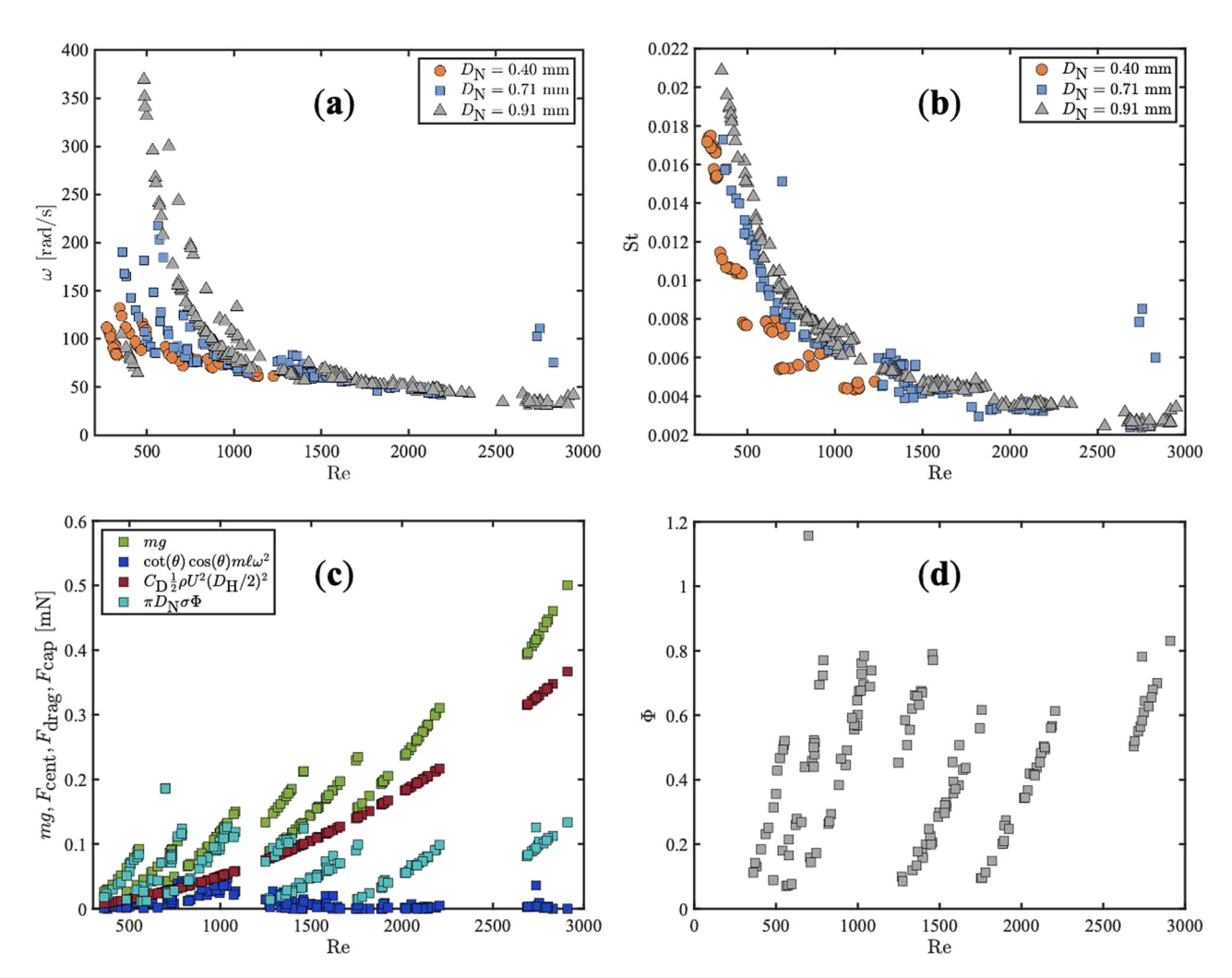


**FIG. 5.** Angular velocity  $\omega$  and Strouhal number St decrease with the Reynolds number. The relation between (a)  $\omega$  and Re and (b) St and Re. Weight, centrifugal, and drag force dictate the magnitude of capillary force. Plot of (c) forces in Eq. (1) and Re and (b)  $\Phi$  and Re.

We nondimensionalize drop angular velocity by an inertial time yielding a modified Strouhal number  $St = \omega D_H/2\pi U$  and plot St vs Re in Fig. 5(b). The Strouhal number in this context represents a ratio between drop angular momentum and the linear momentum of the ascending gas traversing the drop cross section. Thus, the magnitude of St quantifies the momentum transfer from the flow to the drop. Generally, St decreases with increasing Re. Otherwise stated, smaller drops and ascending flow velocities increase the momentum transfer between the gas and the drop. The peaks in St do not correspond to the Re number associated with the peaks in  $\omega$  in Fig. 5(a). Therefore, the angular velocity of a pendant drop is not solely determined by the momentum transfer from the ascending flow to the rotating drop. In conjunction with Fig. 5(a), D<sub>N</sub> has little impact on St for  $Re \ge 1500$ . Below  $Re \approx 1500$ , drops supported by larger needles produce greater Strouhal numbers. The discrepancy in the Strouhal number between drops of like Reynolds number adhered to needles of dissimilar diameters indicates that needle size plays a significant

role in the momentum transfer from the ascending flow to the rotating drop.

We employ the model of a conical pendulum to describe the behavior of rotating pendant drops. In this analogy, the pendulum string tension is replaced by capillary force  $F_{\rm cap}$  acting on the centroid of the pendant drop. Drag force,  $F_{\rm drag}$ , reduces the effective drop weight, resulting in the following force balance along the line of  $\ell$  (Fig. 2).

$$\underbrace{\pi D_{\rm N} \sigma \Phi}_{\rm capillary} + \underbrace{\varepsilon C_{\rm D} \frac{1}{2} \rho U^2 \pi \left(\frac{D_{\rm H}}{2}\right)^2}_{\rm drag} = \underbrace{\cot(\theta) \cos{(\theta)} m \ell \omega^2}_{\rm centrifugal} + \underbrace{mg}_{\rm weight}, \quad (1)$$

where  $\theta$  is the angle between  $\ell$  and the plane perpendicular to the gravitational force acting upon the centroid of the drop,  $\Phi$  is a capillary correction coefficient found within Tate's law, <sup>38</sup> and  $C_D$  is the drag coefficient for a sphere given by the following equation: <sup>39</sup>

$$C_{\rm D} = \frac{24}{\text{Re}} + \frac{0.52 \cdot \text{Re}}{1 + \left(\frac{\text{Re}}{5}\right)^{1.52}} + \frac{0.411(\text{Re} \cdot 2.63 \times 10^{-5})^{-7.94}}{1 + (\text{Re} \cdot 2.63 \times 10^{-5})^{-8}} + \frac{\text{Re} \cdot 0.25 \times 10^{-6}}{1 + \text{Re} \times 10^{-6}}.$$
 (2)

We estimate drag force as that acting on a free-falling sphere modified by a coefficient  $\varepsilon$  to account for non-sphericity and the presence of the needle in the drop wake. Finding a unique pair of  $\varepsilon$  and  $\Phi$  for each trial is intractable. We therefore assume that  $\varepsilon = 1$ , for simplicity, allowing for the computation of capillary force across Re. We plot the relationship between the Reynolds number and the forces of Eq. (1) as well as the corresponding values of  $\Phi$  in Figs. 5(c) and 5(d) for  $D_N = 0.71$ mm. The differences in centrifugal force,  $F_{cent}$ , along Reynolds number contours do not mimic the drastic differences in  $\omega$  observed for Re  $\leq$ 1000 in Fig. 5(a). The relative consistency of centrifugal force across Re is due to inverse relationship between  $\omega$  and  $D_{\rm H}$ . As drop mass increases, angular velocity decreases, resulting in a centrifugal force that is relatively invariant across Re in comparison with weight, capillary, and drag forces. As Re increases, the magnitudes of  $F_{cap}$  and mgbecome disparate as drag dominates the sustaining forces,  $F_{\text{cap}}$  and  $F_{\text{drag}}$ . For fixed U,  $\Phi$  increases with Reynolds number, as shown in Fig. 5(d). We recognize that  $\Phi$  should be less than one. While we expect more consistent  $\Phi$  across Re, the increase in  $\Phi$  along Re contours indicates that either the capillary force is increasing with  $D_{\rm H}$ and/or the increase in  $\Phi$  is accounting for an increase in  $\varepsilon$  (which is treated invariant in our calculations).

We obtain a dimensionless force balance by scaling Eq. (1) by  $\left(D_{\rm H}\sigma\right)^{-1}$ ,

$$\pi \Phi \frac{D_{\mathrm{N}}}{D_{\mathrm{H}}} + \frac{\varepsilon C_{\mathrm{D}} \pi}{8} \operatorname{We}^{*} = \frac{\pi^{3}}{8} \cot(\theta) \cos(\theta) \operatorname{St}^{2} \operatorname{We} + \frac{\pi}{6} \frac{\operatorname{We}}{\operatorname{Fr}}, \quad (3)$$

where We\* =  $\rho_{air}D_{\rm H}U^2/\sigma$  and Fr =  $U^2/gD_{\rm H}$  is the drop Froude number. Solving Eq. (3) for Strouhal number yields

$$St = \left[ \frac{8}{\pi^3 \cot(\theta)\cos(\theta)} \left( \Phi \frac{D_{\rm N}}{D_{\rm H} \text{We}} + \frac{\varepsilon C_{\rm D}}{8} \frac{\text{We}^*}{\text{We}} - \frac{\pi}{6} \frac{1}{\text{Fr}} \right) \right]^{1/2}. \quad (4)$$

300 = 0.40 mm, RST  $D_{\mathrm{N}} = 0.40$  mm, RST  $D_{\mathrm{N}} = 0.71$  mm, RST  $D_{\mathrm{N}} = 0.91$  mm, RST 250  $D_{
m N}=0.40$  mm, HPHON  $D_{\rm N}^{\rm N}=0.71$  mm, HPHON  $D_{\rm N}^{\rm N}=0.91~{
m mm},\,{
m HPHON}$ 200  $D_{\rm N} = 0.40$  mm, Conventional  $D_{\rm N}^{\rm N}=0.71$  mm, Conventional = 0.91 mm, Conventional 150 100 50 0.8 2.4  $\times 10^{-3}$  Solving Eq. (4) for  $\omega$ , we ascertain the following equation:

$$\omega = \left[ \frac{32}{\pi \cot(\theta)\cos(\theta)} \frac{U^2}{D_{\rm H}^2} \left( \Phi \frac{D_{\rm N}}{D_{\rm H} {\rm We}} + \frac{\varepsilon C_{\rm D}}{8} \frac{{\rm We}^*}{{\rm We}} - \frac{\pi}{6} \frac{1}{{\rm Fr}} \right) \right]^{1/2}. \quad (5)$$

For a fixed drop size  $D_{\rm H}$  and flow velocity U, needle diameter  $D_{\rm N}$  determines the magnitude of the Strouhal number in Eq. (4) as We, We\*, and Fr are constant. Large  $D_{\rm N}$  increase the value of St, as observed in Fig. 5(b). An increase in  $D_{\rm H}$  not only increases We, We\*, and Fr decreasing St, but diminishes the impact of  $D_{\rm N}$  [Fig. 5(b)]. We conclude that at Re  $\gtrsim$  1500,  $D_{\rm H}$  is substantially large to overcome the substantive influence of the needle in the wake. Thus, for Re  $\gtrsim$  1500, the ratio describing the transfer of linear momentum from the ascending flow to the rotational momentum of the drop is dominated by the second and third terms in Eq. (4). Likewise, we observe the maximum  $\omega$  is limited by  $D_{\rm N}$  and that large  $D_{\rm N}$  increases drops angular velocity for fixed Re. Larger pendant drops increase We and Fr and thus decrease the magnitude of  $\omega$  as expected.

The use of pendant drops in moving air will likely not be limited to distilled water in future studies. It is thus constructive to probe the usefulness of our analysis by reducing the drop surface tension and altering the repellency of the needle. We, therefore, reduce the surface tension of our drop to 33 mN/m by the inclusion of a surfactant (Sec. II) and film the drops as with distilled water. We reproduce Fig. 5 but using reduced surface tension drops (RST,  $\bigcirc$ ), hydrophobic needles (HPHON,  $\square$ ), and conventional drops ( $\triangle$ ) in Fig. 6.

There is no apparent distinction of St or  $\omega$  between conventional  $(\triangle)$  and  $(\bigcirc, \bigcirc)$  data points in Figs. 6(a) and 6(b). We turn to a one-way ANOVA with a post hoc Tukey's test  $(\hat{\alpha}=0.05)$  to determine whether surface tension and needle modifications are statically significant parameters affecting drop behavior. We present statistical test results in Table I. There are no statistically significant differences for St among the test conditions for the smallest needle. However, drops of reduced surface tension do produce statistically different St for the mid-sized and largest needles. The influence of a hydrophobic needle is significant only for the largest needle, likely a consequence of a longer three-phase contact line. We conclude that as needle size increases, drop oscillation is more sensitive to changes in surface tension and

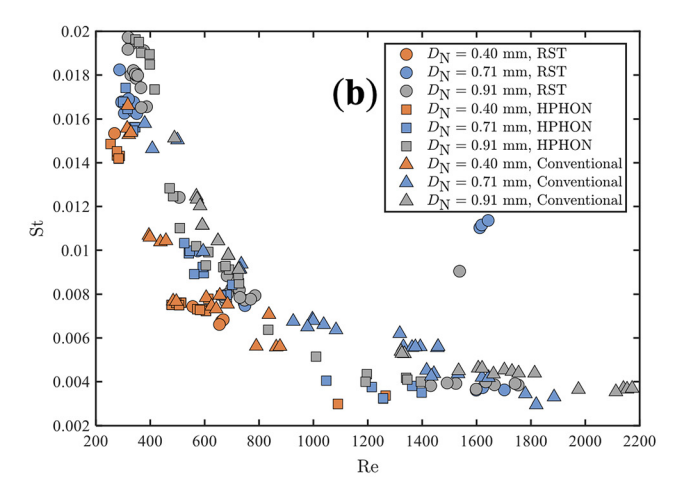


FIG. 6. Effect of effect wettability of needle and reduced surface tension on the relation between ω and (a) Reynolds number, and (b) ℓ for all test needles with diameter D<sub>N</sub>.

**TABLE I.** Analysis of variance (ANOVA) test results for reduced surface tension drops (RST) and hydrophobic needles (HPHON) (p-value: The probability of obtaining the observed results; NS: Not significant, S: Significant).

			p-value	Significance
$D_{\rm N}=0.40~{ m mm}$	Conventional	RST	0.117	NS
		HPHON	0.550	NS
$D_{\rm N}=0.71~{\rm mm}$	Conventional	RST	< 0.001	S
		HPHON	0.057	NS
$D_{\rm N}=0.91~{ m mm}$	Conventional	RST	0.018	S
		<b>HPHON</b>	0.035	S

needle wettability. In each case where changes in surface tension and needle wettability are significant, the magnitude of oscillation decreases.

# V. MAXIMAL PENDANT DROP SIZES ACROSS WINDSPEED

The most massive drop a needle can support before pinch-off is augmented by the presence of ascending airflow. The largest drops supported by a needle of outer diameter  $D_{\rm N}$  in quiescent air have a volume  $V_0=8.6\pm0.3$ ,  $12.2\pm1~\mu$ l, and  $14.9\pm.6~\mu$ l for  $D_{\rm N}=0.4$ , 0.71, and  $0.91~\rm mm$ , respectively. We find the drop volume within  $1~\mu$ l of pinch-off  $V_{\rm max}$  for vertical airflow velocities from  $1-9~\rm m/s$  at  $0.5~\rm m/s$  increments. Drops pinch-off when weight and centrifugal forces exceed the sustaining forces provided by capillary adhesion and aerodynamic drag, as defined in Eq. (1). In the absence of airflow, Eq. (1) reduces to the seminal Tate's law by Harkins and Brown.

To measure the influence of ascending flow upon the maximum drop size a needle can sustain, we create a volumetric ratio between drops of dynamic and ambient conditions  $\vartheta = V_{max}/V_0$ . We plot the relationships between  $\vartheta$  and Re in Fig. 7(a). In general, for Re  $\leq$  1200,  $\vartheta <$  1, such that the maximum drop volume at a given velocity is less than the maximum drop volume at ambient conditions.

Here, the ascending flow is more detrimental to drop adhesion than beneficial; the increased aerodynamic drag is insufficient to counter the magnitude of flow-induced rotation. We plot angular velocity  $\omega$  vs Re in Fig. 7(b). The peak in angular velocity corresponds to a minimum in drop volume as denoted by the vertical lines in Figs. 7(a) and 7(b). Above Re  $\geq$  480, an increase in  $\vartheta$  is associated with a decrease in  $\omega$ . Once  $\vartheta > 1$ , aerodynamic drag is sufficient to counter the decreasing magnitude of centrifugal force. Larger drops rotate more slowly, particularly for Re  $\geq$  1200, as previously shown in Fig. 5(a).

The needle diameter of a pendant drop influences the largest drop volume attainable for a given velocity. The minimum and maximum of  $\vartheta$  are observed for our smallest test needle  $D_{\rm N}=0.41$  mm, as seen in Fig. 7(a). Larger needles support drops of greater volume due to an increased capillary force. Above Re  $\approx$  1300, maximally sized drops adhered to large needles rotate at greater angular velocities. The increase in capillary force allows for greater  $\omega$ , as the angular velocity and drop mass requisite for pinch-off increase, as shown in Eq. (1). Below Re  $\approx$  1300, the increase in  $\omega$  for small needles is likely the consequence of wake structure changes due to needle diameter.

#### VI. CHARACTERISTIC SHAPE AND SWEPT VOLUME

The shape of a pendant drop may be static or deforming as it rotates about the needle on either a static or dynamic axis (Sec. III). To address the complexity birthed by periodic shape deformation, static, and dynamic axes, we introduce a static, characteristic shape representative of our highly dynamic drops. The characteristic shape of a pendant drop is the profile of the aggregated binarized shadow graph (ABS) of which the resulting volume  $V_{\rm C}$  matches the volume of the oscillating drop V. Characteristic drop contours (right) are shown beside their corresponding ABS (left) in Fig. 8. Characteristic shapes unify otherwise disparate drop behavioral modes, as demonstrated by the visual similarity in characteristic drop shape across the six dynamic modes. The characteristic drop volume permits the determination of swept volumetric flow rate, the rate at which a volume of air is swept by the pendant drop as the air ascends in our tunnel

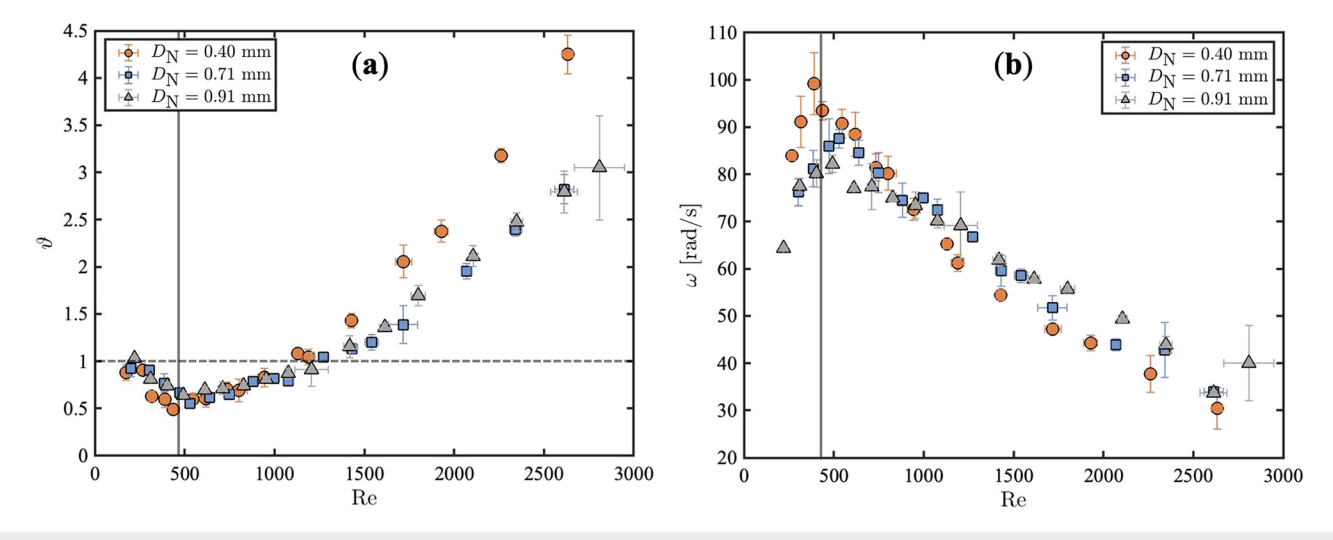
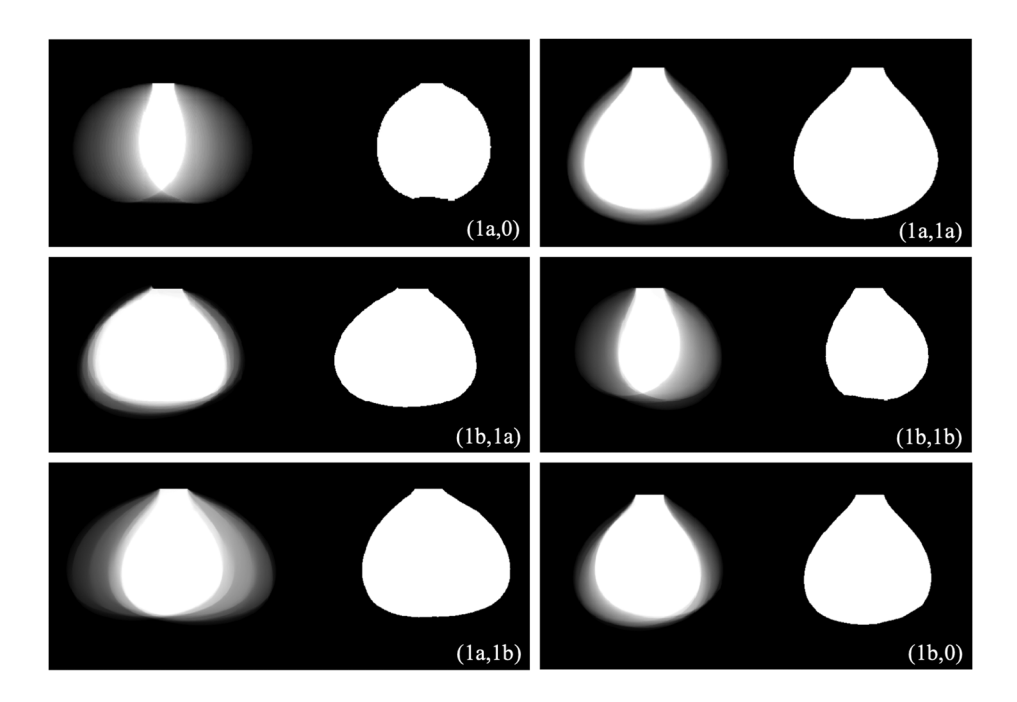


FIG. 7. Ascending airflow induces pendant drop rotation and modulates the largest drop a needle can sustain. (a) The relation between non-dimensional maximum volume  $\vartheta$  and Reynolds number. (b) The relation between angular velocity  $\omega$  and Reynolds number of the largest drops a needle can sustain.



**FIG. 8.** Typical ABS and derived characteristic shapes for each oscillatory mode.

$$\dot{V}_{\rm S} = U\pi (D_{\rm C}/2)^2,\tag{6}$$

where  $D_{\rm C}$  is the maximum diameter of the characteristic drop. We diagram the swept volume  $V_{\rm S}$  carved out by a characteristic, static drop in Fig. 9(a). We demonstrate characteristic drop shapes are good representations of actual drops by comparing the magnitude of the Reynolds number of the original drop to the characteristic drop diameter Re<sub>C</sub> and find 0.88 < Re/Re<sub>C</sub> < 1.08 across all Re tested, as shown in Fig. 9(b). We note that the ratio Re/Re<sub>C</sub> is equivalent to a ratio of diameters  $D_{\rm H}/D_{\rm C}$ .

We plot the relationship between  $\dot{V}_S$  and Reynolds number of the original drop in Fig. 9(c). The swept volumetric flow rate of characteristic drops increases with the Reynolds number. The collapse of our data in Fig. 9(c) shows that  $\dot{V}_S$  is only a function of Re of the original drop, and can be predicted without regard for needle size, oscillation frequency, and behavioral mode. In other words, future researchers can well estimate  $\dot{V}_S$  without the need to find a characteristic drop  $D_C$ .

The efficacy of a particularly sized drop to sweep a passing flow can be quantified by a ratio of  $\dot{V}_S$  and drop volume V, a quantity we term swept frequency,

$$f_{\rm S} = \frac{\dot{\mathcal{V}}_{\rm S}}{\mathcal{V}} \sim \frac{U}{D_{\rm H}},\tag{7}$$

noting that  $D_C \approx D_H$ . We plot  $f_S$  vs Re in Fig. 9(d). The efficacy of a given drop to sweep a fixed ascending flow scales with  $1/D_H$ , as shown by the velocity contours in Fig. 9(d). The upper and lower visual bounds of  $f_S$  correspond to the limit for a drop to remain on the needle extremity during experimentation. Above the dashed curve in Fig. 9(d), drop weight is insufficient to counter the aerodynamic drag and drops are pushed up along the needle shaft. Liquids of greater density will push this boundary of pendant behavior northeast. Below the solid curve in Fig. 9(d), pinch-off conditions are met as weight and

centrifugal force overcome drag and capillary force (Sec. IV). Liquids of greater density will move the pinch-off boundary northwest.

#### VII. DISCUSSION

We categorize pendant drop behavior in ascending flows into seven behavioral modes according to their rotational axis and periodic deformation of shape. Of the six dynamic modes, needle diameter, ascending flow velocity, and drop size greatly influence the angular velocity of the drop. Using an ABS, we present a characteristic shape representative of our dynamic drop, by which we calculate a swept volumetric flow rate of air and the efficacy of a drop to sweep the passing flow. In addition to drop rotation, the needle diameter plays a significant role in the drop size a needle can support under a given flow condition. We predict that for some  $D_{\rm N} > 0.91\,{\rm mm}$ , greater angular velocities would be observed below Re < 1500—drops oscillate faster on larger needles. Drops adhered to smaller needles  $D_{
m N} < 0.41~{
m mm}$ would likely rotate at lower angular velocities. As a result, needles smaller than those considered here may prove to be superior supports in studies where pendant drops are used to mimic free-falling raindrops.

The cause for lower angular velocities by smaller needles is likely a consequence of wake dynamics. The oscillation of a tethered sphere provides the most studied analog to our pendant drops because tethered spheres oscillate in a steady, uniform flow as a result of wake dynamics. Oharacteristics of sphere wakes can be characterized simply by a Reynolds number. Here, our quasi-spherical drops are tethered to their needles and are free to oscillate by the forcing wake. Aside from drop propensity for deformation, the major difference between a classical tethered sphere and our drops is the occlusion of the wake structure by the needle. It follows that larger needles provide a greater obstruction to wake forcing via vortex shedding. The reduction of the drop surface area on which adverse pressure acts likely

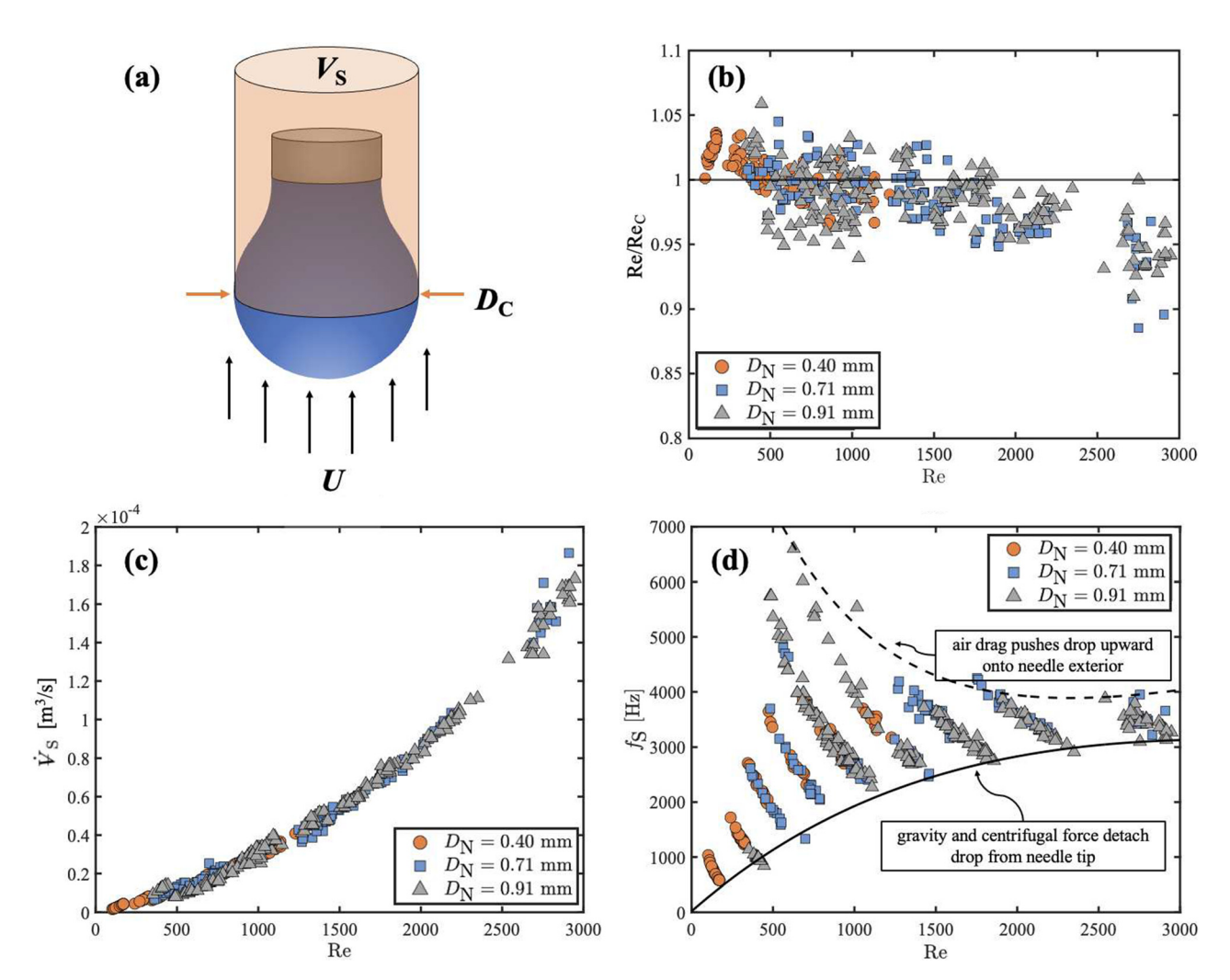


FIG. 9. Characteristic shape simplifies swept volume. (a) Diagram showing swept volume,  $V_S$ . Plots of (b) Re/Re<sub>C</sub> vs Re. (c)  $\dot{V}_S$  vs Re, and (d)  $f_S$  vs Re.

disrupts vortex properties. Larger needles likely increase the vortex shedding frequency for  $500 \lesssim \text{Re} \lesssim 1500$ , as evidenced by Fig. 5(a). The augmentation of wake structure behind pendant drops by tethering needles is a fruitful area for future investigation and will likely be the domain of computational studies.

Changing needle sizes also has implications in a force balance in terms of capillary and drag force. In this study, we assume that the drag force on pendant drops is equivalent to the drag on a free-falling sphere. Equating  $\varepsilon=1$  in Eq. (1) leads to a range of capillary correction coefficients  $\Phi$  [Fig. 5(d)] that we expect should have less variance across Re. Furthermore, the values of  $\Phi>1$  returned by a force balance are nonphysical, which indicates that  $\varepsilon$  is a function of the Reynolds number. A unique pair of  $\Phi$  and  $\varepsilon$  for every trial that satisfies Eq. (1) is difficult to ascertain and fruitful area for simulation studies.

The shape and therefore drag on raindrops has been the subject of numerous studies. <sup>20,43,44</sup> Much like pendant drops, raindrops experience shape oscillations. <sup>26</sup> The cross-sectional area of a large raindrop in the falling direction is treated as circular in models devised by

Szakall et al.,<sup>20</sup> Beard and Chuang,<sup>43</sup> and Pruppacher and Pitter.<sup>44</sup> We too find that characteristic shape of pendant drop cross-sectional area is likewise circular, such that the swept volume and swept frequency of pendant drops and raindrops will be comparable at fixed Reynolds number. Due to the similarities between pendant drops and raindrops in this regard, pendant drops provide an experimental centerpiece by which to further the field of atmospheric science. Earth's restorative processes to remove atmospheric aerosols include settling, nucleate scavenging, and below-cloud precipitate scavenging<sup>45</sup>—a process by which precipitation brings aerosol particles to the Earth's surface, acting as the most efficient aerosol sink. 46,47 Despite this efficiency, little is known about the physics that drive wet deposition, and there exists little experimental evidence demonstrating the collection efficiency of falling drops. We believe that a natural first step in experimentation is the exposure of pendant drops to aerosol-rich flows. Furthermore, we posit that the swept volume of air and swept frequency of a pendant drop provide a foundation by which future analysis concerning precipitate scavenging via pendant drops may be built.

#### VIII. CONCLUSION

We observe the dynamics of pendant drops in a pull-type vertical wind tunnel. Drop oscillation is captured via a high-speed camera for a drop Reynolds number Re = 200-3000, where we investigate the influence of drop size, needle diameter, and ascending flow velocity on drop behavior. Exposed to ascending flows, drops exhibit seven behavioral modes characterized by rotational path and periodic shape deformation. The predominant behavioral mode exhibited by our drops across all flow velocities is the one in which behavior is described solely by rotation about a static axis without deforming in cross section. At high flow velocities, U = 8-9 m/s, drop behavior becomes increasingly dynamic as drops are more likely to periodically deform and/or rotate about a dynamic axis. For drop modes characterized by periodic shape deformations, the amplitude of oscillation of the drop centroid is less than the needle diameter. Drops oscillate at angular velocities dictated by Reynolds number and needle diameter. Angular velocity decreases with increasing drop size and for Re ≤ 1300 drops oscillate faster when adhered to larger needles. The ratio of the angular momentum of the drop to the linear momentum of the airflow, captured by a modified Strouhal number, is highest for drops of low Re. Through drag and centrifugal forces, the presence of wind alters the maximally sized drop a needle can sustain. We observe a dip in the largest drop a needle can sustain for velocities that produce Re ≤ 1200. Normalizing aggregated video frames of binarized drops permits the generation of static characteristic shapes of dynamic drops. Such shapes permit the calculation of the swept volume of air intercepted by oscillating drops. The rate at which a pendant drop sweeps volume is only a function only of the Reynolds number of the original drop and can be predicted without regard for needle size, oscillation frequency, and behavioral mode.

#### **ACKNOWLEDGMENTS**

We thank the National Science Foundation (Grant No. GEO-2201828) for their support, and Kyle Fagin, Hayley Kopish, Bailey Gadams, and Bryce Jardret for experimental efforts.

### AUTHOR DECLARATIONS

### Conflict of Interest

The authors have no conflicts to disclose.

#### **Author Contributions**

Jacob D. Dockery: Data curation (lead); Formal analysis (lead); Investigation (equal); Methodology (supporting); Software (lead); Validation (lead); Visualization (lead); Writing – original draft (equal); Writing – review & editing (equal). Duygu Yilmaz Aydin: Data curation (equal); Investigation (equal); Validation (supporting); Writing – original draft (supporting); Writing – review & editing (supporting). Andrew Keith Dickerson: Conceptualization (lead); Funding acquisition (lead); Investigation (equal); Project administration (lead); Resources (lead); Supervision (lead); Writing – original draft (equal); Writing – review & editing (equal).

#### DATA AVAILABILITY

The data that support the findings of this study are openly available in perpetuity via Open Science Framework at https://osf.io/ufwez/, Ref. 48.

#### **REFERENCES**

- <sup>1</sup>M. A. Kandadai, P. Mohan, G. Lin, A. Butterfield, M. Skliar, and J. J. Magda, "Comparison of surfactants used to prepare aqueous perfluoropentane emulsions for pharmaceutical applications," Langmuir **26**, 4655–4660 (2010).
- <sup>2</sup>A. Schmit, L. Courbin, M. Marquis, D. Renard, and P. Panizza, "A pendant drop method for the production of calibrated double emulsions and emulsion gels," RSC Adv. 4, 28504–28510 (2014).
- gels," RSC Adv. 4, 28504-28510 (2014).

  <sup>3</sup>P. J. Wilde, G. Garcia-Llatas, M. J. Lagarda, R. P. Haslam, and M. M. Grundy,
  "Oat and lipolysis: Food matrix effect," Food Chem. 278, 683-691 (2019).
- <sup>4</sup>J. Maldonado-Valderrama, T. del Castillo-Santaella, M. J. Gálvez-Ruiz, J. A. Holgado-Terriza, and M. Á. Cabrerizo-Vílchez, "Structure and functionality of interfacial layers in food emulsions," in *Food Structure and Functionality* (Elsevier, 2021), pp. 1–22.
- <sup>5</sup>E. Y. Arashiro and N. R. Demarquette, "Use of the pendant drop method to measure interfacial tension between molten polymers," Mat. Res. 2, 23–32 (1999).
- <sup>6</sup>N. Zobeiry and C. Duffner, "Measuring the negative pressure during processing of advanced composites," Compos. Struct. 203, 11–17 (2018).
- <sup>7</sup>P. A. Rühs, L. Böcker, R. F. Inglis, and P. Fischer, "Studying bacterial hydrophobicity and biofilm formation at liquid–liquid interfaces through interfacial rheology and pendant drop tensiometry," Colloids Surf., B 117, 174–184 (2014).
- <sup>8</sup>S. S. Yadav, B. S. Sikarwar, P. Ranjan, and R. Janardhanan, "Microfluidic system for screening disease based on physical properties of blood," Bioimpacts **10**, 141 (2019).
- <sup>9</sup>M. J. Fuerstman, A. Lai, M. E. Thurlow, S. S. Shevkoplyas, H. A. Stone, and G. M. Whitesides, "The pressure drop along rectangular microchannels containing bubbles," Lab Chip 7, 1479–1489 (2007).
- <sup>10</sup>C. Clanet and J. Lasheras, "Transition from dripping to jetting," J. Fluid Mech. 383, 307–326 (1999).
- <sup>11</sup>D. Henderson, W. Pritchard, and L. Smolka, "On the pinch-off of a pendant drop of viscous fluid," Phys. Fluids 9, 3188 (1997).
- <sup>12</sup>J. P. Garandet, B. Vinet, and P. Gros, "Considerations on the pendant drop method: A new look at Tate's law and Harkins' correction factor," J. Colloid Interface Sci. 165, 351–354 (1994).
- <sup>13</sup>L. M. Parkinson and C. M. Phan, "Natural vibration of an aqueous pendant drop," Exp. Therm. Fluid Sci. 90, 48–54 (2018).
- <sup>14</sup>M. A. Quetzeri-Santiago, I. W. Hunter, D. Van Der Meer, and D. F. Rivas, "Impact of a microfluidic jet on a pendant droplet," Soft Matter 17, 7466–7475 (2021).
- <sup>15</sup>R. Wang and X. Li, "On the effective surface tension of powder-derived liquid marbles," Powder Technol. 367, 608 (2020).
- <sup>16</sup>E. Bormashenko, A. Musin, G. Whyman, Z. Barkay, A. Starostin, V. Valtsifer, and V. Strelnikov, "Revisiting the surface tension of liquid marbles: Measurement of the effective surface tension of liquid marbles with the pendant marble method," Colloids Surf., A 425, 15–23 (2013).
- <sup>17</sup>B. Zhang, Y. Ling, P.-H. Tsai, A.-B. Wang, S. Popinet, and S. Zaleski, "Short-term oscillation and falling dynamics for a water drop dripping in quiescent air," Phys. Rev. Fluids 4, 123604 (2019).
- <sup>18</sup>R. J. Kubesh and K. V. Beard, "Laboratory measurements of spontaneous oscillations for moderate-size raindrops," J. Atmos. Sci. 50, 1089–1098 (1993).
- <sup>19</sup>F. Testik and A. P. Barros, "Toward elucidating the microstructure of warm rainfall: A survey," Rev. Geophys. 45, RG2003, https://doi.org/10.1029/2005RG000182 (2007).
- <sup>20</sup>M. Szakáll, K. Diehl, S. K. Mitra, and S. Borrmann, "A wind tunnel study on the shape, oscillation, and internal circulation of large raindrops with sizes between 2.5 and 7.5 mm," J. Atmos. Sci. 66, 755–765 (2009).
- <sup>21</sup>M. Szakáll, S. Kessler, K. Diehl, S. K. Mitra, and S. Borrmann, "A wind tunnel study of the effects of collision processes on the shape and oscillation for moderate-size raindrops," Atmos. Res. 142, 67–78 (2014).
- <sup>22</sup>M. Szakáll and I. Urbich, "Wind tunnel study on the size distribution of droplets after collision induced breakup of levitating water drops," Atmos. Res. 213, 51–56 (2018).
- <sup>23</sup>S. Müller, M. Szakáll, S. K. Mitra, K. Diehl, and S. Borrmann, "Shapes and oscillations of raindrops with reduced surface tensions: Measurements at the Mainz vertical wind tunnel," Atmos. Res. 119, 38–45 (2013).
- <sup>24</sup>M. Szakáll, M. Debertshäuser, C. P. Lackner, A. Mayer, O. Eppers, K. Diehl, A. Theis, S. K. Mitra, and S. Borrmann, "Comparative study on immersion

- freezing utilizing single-droplet levitation methods," Atmos. Chem. Phys. 21, 3289-3316 (2021).
- 25D. N. Gabyshev, M. Szakáll, D. V. Shcherbakov, A. A. Fedorets, and S. M. Dyachkov, "Oscillatory signatures in the raindrop motion relative to the air medium with terminal velocity," Atmosphere 13, 1137 (2022).
- <sup>26</sup>M. Szakáll, S. K. Mitra, K. Diehl, and S. Borrmann, "Shapes and oscillations of falling raindrops—A review," Atmos. Res. 97, 416-425 (2010).
- <sup>27</sup>K. V. Beard, V. Bringi, and M. Thurai, "A new understanding of raindrop shape," Atmos. Res. 97, 396-415 (2010).
- <sup>28</sup>E. D. Wilkes and O. A. Basaran, "Forced oscillations of pendant (sessile) drops," Phys. Fluids 9, 1512-1528 (1997).
- <sup>29</sup>O. A. Basaran and D. W. DePaoli, "Nonlinear oscillations of pendant drops," Phys. Fluids 6, 2923-2943 (1994).
- 30 A. S. Mohamed, J. M. Lopez-Herrera, M. A. Herrada, L. B. Modesto-Lopez, and A. M. Ganan-Calvo, "Effect of a surrounding liquid environment on the electrical disruption of pendant droplets," Langmuir 32, 6815-6824 (2016).
- <sup>31</sup>N. Zografov, N. Tankovsky, and A. Andreeva, "Droplet oscillations driven by an electric field," Colloids Surf., A 460, 351-354 (2014).
- 32 A. Andreeva and N. Zografov, "Oscillation mode and resonant frequencies of spherical pendant droplets," AIP Conf. Proc. 2075, 160015 (2019).
- <sup>33</sup>J. H. Moon, B. H. Kang, and H.-Y. Kim, "Effects of acoustic resonance on hydrodynamics and evaporation of a pendant liquid droplet," in International Electronic Packaging Technical Conference and Exhibition (ASME, 2005), Vol. 42002, pp. 2005-2009.
- 34J. H. Moon, B. H. Kang, and H.-Y. Kim, "The lowest oscillation mode of a pendant drop," Phys. Fluids 18, 021702 (2006).
- 35 A. Bussonnière, M. Baudoin, P. Brunet, and O. B. Matar, "Dynamics of sessile and pendant drops excited by surface acoustic waves: Gravity effects and correlation between oscillatory and translational motions," Phys. Rev. E 93, 053106

- 36J. Sargison, G. Walker, and R. Rossi, "Design and calibration of a wind tunnel with a two dimensional contraction," in 15th Australasian Fluid Mechanics
- <sup>37</sup>L. Sigalotti, F. Peña-Polo, and L. Trujillo, "An image analysis procedure for measuring the surface tension of pendant micro-drops," J. Comput. Methods 12, 371-382 (2012).
- $^{38}$ W. Harkins and F. Brown, "The determination of surface tension (free surface energy), and the weight of falling drops: The surface tension of water and benzene by the capillary height method," J. Am. Chem. Soc. 41, 499-524 (1919).
- <sup>39</sup>F. A. Morrison, An Introduction to Fluid Mechanics (Cambridge University Press, 2013).
- <sup>40</sup>C. Williamson and R. Govardhan, "Dynamics and forcing of a tethered sphere in a fluid flow," J. Fluids Struct. 11, 293-305 (1997).
- <sup>41</sup>R. Govardhan and C. Williamson, "Vortex-induced motions of a tethered sphere," in Proceedings of the 3rd International Colloquium on Bluff Body Aerodynamics and Applications, 1996 [J. Wind Eng. Ind. Aerodyn. 69-71, 375-385 (1997)].
- <sup>42</sup>H. Sakamoto and H. Haniu, "A study on vortex shedding from spheres in a uniform flow," J. Fluids Eng. 112, 386-392 (1990).
- <sup>43</sup>K. V. Beard and C. Chuang, "A new model for the equilibrium shape of raindrops," J. Atmos. Sci. 44, 1509-1524 (1987).
- 44H. R. Pruppacher and R. L. Pitter, "A semi-empirical determination of the shape of cloud and rain drops," J. Atmos. Sci. 28, 86-94 (1971).
- <sup>45</sup>D. Liu, C. He, J. P. Schwarz, and X. Wang, "Lifecycle of light-absorbing carbo-
- naceous aerosols in the atmosphere," Clim. Atmos. Sci. 3, 1–18 (2020). 46J. Henzing, D. Olivié, and P. Van Velthoven, "A parameterization of size resolved below cloud scavenging of aerosols by rain," Atmos. Chem. Phys. 6, 3363 (2006).
- <sup>47</sup>C. Andronache, "Estimated variability of below-cloud aerosol removal by rainfall for observed aerosol size distributions," Atmos. Chem. Phys. 3, 131-143 (2003).
- <sup>48</sup>A. Dickerson and J. Dockery (2023). "Pendant drops in vertical airflow," Open Science Framework, osf.io/ufwez